

Anharmonic vibrational relaxation dynamics for a molecular impurity mode in alkali halide crystals

W. E. Moerner

IBM Research Laboratory, San Jose, California 95193

A. R. Chraplyvy

AT&T Bell Laboratories, Crawford Hill, Holmdel, New Jersey 07733

A. J. Sievers

Laboratory of Atomic and Solid State Physics, Cornell University, Ithaca, New York 14853

(Received 21 December 1983)

High-resolution diode-laser spectroscopy and the nonequilibrium techniques of incoherent laser saturation and transient hole-burning spectroscopy have been used to measure the relaxation dynamics (specifically T_1 and T_2) of the ν_3 internal vibrational mode of ReO_4^- molecules as functions of temperature and host alkali halide lattice. Inhomogeneously broadened linewidths less than 0.02 cm^{-1} were observed in annealed crystals at low temperatures. To retrieve the homogeneous linewidths from the inhomogeneously broadened lines, hole-burning measurements of T_2 were performed with the use of a CO_2 laser as a saturating pump and either a Pb-salt diode laser or another CO_2 laser as a tunable probe. Holes as narrow as 10 MHz (full width at half maximum) were observed in inhomogeneously broadened lines several cm^{-1} wide. Excited-state lifetimes T_1 were measured by CO_2 -laser saturation measurements, which provide values for the saturation intensity I_s , and hence the product $T_1 T_2$. Above 10 K the dominant dephasing (T_2) mechanism is acoustic-phonon scattering, whereas below 10 K T_2 achieves the fundamental upper limit of $2T_1$, signifying that dephasing is lifetime limited. The results of a systematic study of the alkali halide host lattice dependence of the excited-state decay rate at low temperatures show that the decay channel consists of multistep emission of lower-energy internal modes, localized phonon modes, and band phonons.

I. INTRODUCTION

In 1970, Gethins¹ predicted from a first-principles numerical calculation that the high-frequency local mode for the H^- center in KBr (447 cm^{-1}) would have an intrinsic linewidth of 10^{-4} cm^{-1} (3 MHz) due to three- and four-phonon decay processes. Laser-excited vibrational fluorescence studies of CO molecules matrix-isolated in solid Ar showed that the vibrational decay at 2100 cm^{-1} occurs primarily by photon emission and not by nonradiative decay.^{2,3} At the other extreme, laser-saturation measurements⁴ on the local-mode system $\text{CaF}_2:\text{H}^-$ at 90 K show picosecond decay times indicative of multiphonon relaxation. Because the multiphonon relaxation rate should decrease exponentially with increasing ratio of vibrational-mode frequency to phonon frequency while the radiative relaxation rate should increase as the cube of the vibrational mode frequency, a window with long relaxation times is expected for ir-active vibrational modes in the 1000-cm^{-1} region.

This paper describes the systematic study in the 1000-cm^{-1} region of the vibrational relaxation dynamics of ReO_4^- molecules matrix-isolated in alkali halide lattices. The relaxation processes can be characterized by two relaxation lifetimes of the excited state, namely, the energy relaxation lifetime T_1 and the (homogeneous) dephasing time T_2 . High-resolution linear spectroscopy and the nonequilibrium techniques of laser saturation and tran-

sient hole-burning spectroscopy over a wide temperature range have been utilized to understand the microscopic mechanisms responsible for T_1 and T_2 in various alkali halide lattices. The intrinsic symmetry and simplicity of this hole-burning system has enabled us to deduce many properties of the anharmonic decay processes and to predict that other defect modes in solids may have vibrational Q 's as large as 10^{12} . Preliminary reports on incoherent laser saturation,⁵ the temperature dependence of the homogeneous linewidth (T_2),^{6,7} and the lattice dependence⁸ of T_1 and T_2 have already appeared. This paper is intended to explain these measurements and the corresponding conclusions in detail. It is important to note that *persistent* hole burning (as opposed to the transient hole burning reported here) has also been observed for this system.⁹

Section II serves as a general summary of the properties of ReO_4^- molecules doped into alkali halide crystals. Emphasis is placed on linear high-resolution spectroscopy in the ν_3 internal-mode region. Section III describes the experimental methods and data-reduction techniques that were used to measure the relaxation times T_1 and T_2 . Section IV presents the results of the T_1 and T_2 measurements and Sec. V discusses the origins of the various relaxation processes. Utilizing the systematic variation of the relaxation rates from alkali halide to alkali halide, we observe that lower-frequency internal modes of the molecule and even-symmetry local-phonon modes are critical

to the understanding of the anharmonic decay channel. We conclude in Sec. V that although the ReO_4^- molecular ion exhibits fairly fast nonradiative decay rather than radiative emission with long lifetimes, the reasons for this follow from the details of the decay mechanism. If one considers a molecule-lattice system in which the lowest-frequency vibrational mode is probed, no local modes are present and no free-rotor motion is allowed, the vibrational Q should approach 10^{12} . In fact, recent results on CN^- in alkali halides¹⁰ show vibrational emission and long lifetimes in partial support of this conclusion.

II. ReO_4^- -DOPED ALKALI HALIDE CRYSTALS

The properties of both the lattices and the dopant played pivotal roles in unraveling the relaxation dynamics of a polyatomic molecule in a solid host. The use of an ordered solid for matrix isolation, especially an alkali halide, has distinct advantages. For example, the phonon dispersion curves for such hosts have been measured.¹¹ This means that the influence of lattice phonons on the molecular relaxation mechanisms can be studied in a well-defined manner, as opposed to the situation with amorphous hosts having ill-defined phonon spectra. Furthermore, alkali halides offer substitutional sites with high point-group symmetry, which allows most molecules to retain their free-molecule vibrational modes. In addition, alkali halides are stable at room temperature, which facilitates temperature-dependent measurements over wide temperature ranges.

The ReO_4^- molecule was chosen for this study because the ν_3 vibrational-mode absorption lies in the frequency range spanned by the CO_2 laser. Although the ν_3 -mode absorption occurs near $10.7 \mu\text{m}$, CO_2 -laser-line coincidences are difficult to produce because the CO_2 laser is not continuously tunable and the ReO_4^- absorption line is very narrow at low temperatures. Another characteristic

of ReO_4^- molecules is stability at the temperatures required for the growth of alkali halide single crystals. Consequently, the molecules can be incorporated into the host by simple addition to the melt. A third special feature of these molecules is their tetrahedral symmetry. This relatively high symmetry greatly reduces the number of distinct orientations of the molecule in the lattice as compared to the case with molecules of lower symmetry. Finally, the molecule is monovalent, allowing substitutional doping without the need for vacancies to maintain local charge neutrality.

Several physical properties of the ReO_4^- molecule are listed in Table I. The molecule has an effective ionic radius of 2.7 \AA , which is larger than the ionic radii of the halogens for which the molecule substitutes (I^- , 2.19 \AA ; 1.95 \AA ; Cl^- , 1.89 \AA). The result is that the molecule barely fits into the host lattice, and steric effects are expected to be important. A careful study of infrared and Raman frequencies for ReO_4^- ions in various alkali halide lattices¹⁷ leads to the conclusion that the molecule retains its tetrahedral symmetry in the host. There are only two distinct symmetry-preserving orientations of a tetrahedral molecule at an octahedral site. This fact together with the observation that the oxygen atoms protrude from the molecule leads to the expectation that the $\text{Re}-\text{O}$ bonds orient themselves along the $\langle 111 \rangle$ body diagonals (assuming all of the O atoms have the same atomic weight). Furthermore, due to the large size of the ion, one would expect rotational motion to be strongly inhibited.

The ReO_4^- molecule has four normal vibrational modes with frequencies given in Table I. These normal modes and their symmetries are illustrated at the top of Fig. 1. All four modes are Raman active, and the ν_3 and ν_4 modes are also infrared active. A room-temperature infrared spectrum of RbI heavily doped with ReO_4^- molecules is shown in the lower part of the figure. In addi-

TABLE I. Properties of the ReO_4^- molecule (specifically, $^{185}\text{Re}^{16}\text{O}_4^-$ and $^{187}\text{Re}^{16}\text{O}_4^-$. Unless stated otherwise, all properties were taken from Ref. 12).

Natural abundance (^{187}Re : ^{185}Re)	63%:37%
Total electronic spin S	0
Total orbital angular momentum L	0
Total nuclear spin I	0
Nuclear quadrupole moment Q	$2.7 \text{ b } ^{185}\text{Re}$ $2.6 \text{ b } ^{187}\text{Re}$
Ionic radius	2.7 \AA^a
Molecular weight (natural ReO_4^-)	250.2 amu
Rotational constant B	$\sim 0.1 \text{ cm}^{-1b}$
Effective mass of ν_3 mode	14.5 amu ^c
Dipole moment of ν_3 mode, $ \vec{\mu} $	$3.4 \times 10^{-19} \text{ esu cm}^d$
Free-ion frequencies of vibrational modes: ^e	
ν_1	971 cm^{-1}
ν_2	331 cm^{-1}
ν_3	918 cm^{-1}
ν_4	331 cm^{-1}

^aSee Ref. 13.

^bEstimated from B for OsO_4 (0.13 cm^{-1}), from Ref. 14.

^cFrom Ref. 15.

^dSee Appendix A.

^eFrom Ref. 16.

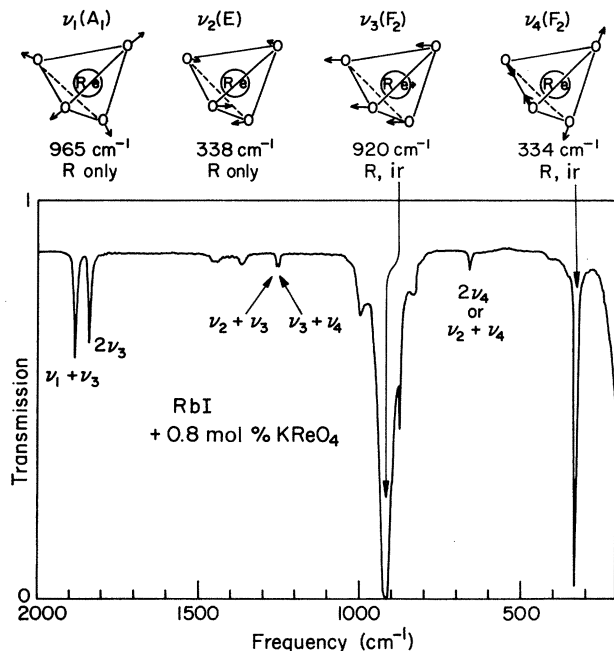


FIG. 1. Normal modes of the ReO_4^- molecule. All four modes are Raman active and ν_3 and ν_4 are also infrared active. A room-temperature spectrum of ReO_4^- molecules in RbI is shown in the lower part of the figure. Resolution $\approx 1 \text{ cm}^{-1}$.

tion to the two infrared-active-mode absorptions, various combination lines can be observed. The sharp absorption just to the low-frequency side of the ν_3 line is due to the ^{18}O isotope.

We note that the ν_3 frequency falls in the P branch of the $10.6\text{-}\mu\text{m}$ band of the CO_2 laser. Figure 2 shows the ν_3 -mode frequency for a variety of alkali halide lattices at room temperature. In general, as the lattice size de-

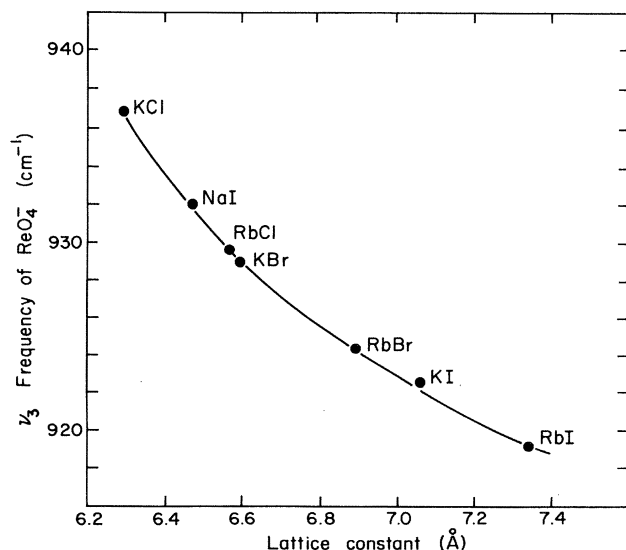


FIG. 2. ReO_4^- ν_3 -mode frequency at room temperature versus host lattice constant. The solid line is a guide to the eye.

creases, the mode shifts toward higher frequencies. In addition, steric effects in the smaller lattices limit the ReO_4^- concentrations that can be achieved, which prevents observation of all the combination lines in these hosts.

Although the ν_3 mode of ReO_4^- in alkali halides falls in the range of CO_2 -laser frequencies, laser excitation of this mode at low temperatures is virtually impossible in most pure-host crystals. The absorption linewidth is strongly temperature dependent and at low temperatures the linewidths are less than 0.02 cm^{-1} . To illustrate this, Fig. 3 shows an extremely-high-resolution ($3 \times 10^{-4} \text{ cm}^{-1}$) diode-laser absorption spectrum⁶ of unannealed and annealed KI + 0.001 mol % KReO_4 at 2 K. The spectrum of the unannealed sample in part (a) of the figure shows a splitting of the ν_3 mode into three unresolved components. However, upon annealing [part (b) of Fig. 3], the structure disappears, indicating that the splitting may have been due to excessive strains introduced during the growth process. The inhomogeneously broadened ν_3 absorption is 0.016 cm^{-1} wide [full width at half maximum (FWHM)] in the annealed host. Now, since the CO_2 -laser-line spacing is about 2 cm^{-1} , the probability of a coincidence between the ν_3 -mode absorption and a CO_2 -laser line is quite small. In fact, aside from heavily doped RbI there are no known low-temperature coincidences when ReO_4^- is the sole impurity in an alkali halide. This problem can be remedied by adding a second cation dopant (e.g., Na^+ , Rb^+ , or Cs^+ in potassium halides; Na^+ , K^+ , or Cs^+ in rubidium halides, etc.) to the ReO_4^- -doped alkali halide lattice.⁵ The second dopant inhomogeneously strain-broadens or splits the ReO_4^- ν_3 absorption line. The inhomogeneous broadening in these alloy hosts is on the order of $1\text{--}2 \text{ cm}^{-1}$ and therefore it is

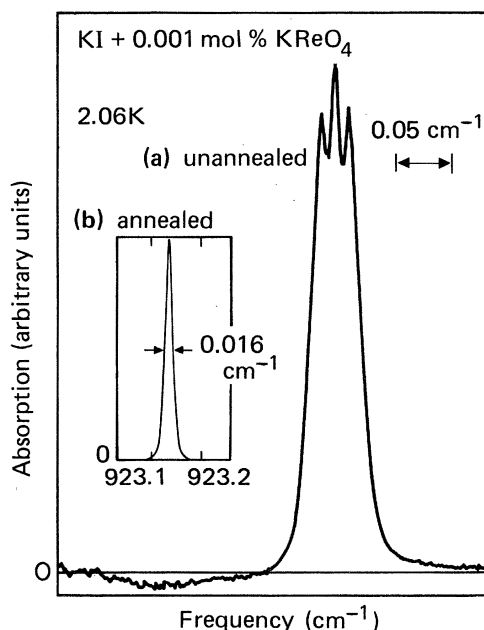


FIG. 3. Diode-laser absorption spectrum of (a) unannealed and (b) annealed KI + 0.001 mol % KReO_4 at 2 K.

relatively easy to find a CO₂-laser line coinciding with some part of the ν_3 absorption.

These alloy hosts yield unusual spectra for the ν_3 -mode absorption. Figure 4 shows a high-resolution¹⁸ transmission spectrum of annealed RbI + 0.05 mol % KReO₄ at 28 K. The two strong lines are due to the two Re isotopes. The various satellite lines are due to strain gradients and defects caused by the presence of the foreign K⁺ cations. The ReO₄⁻ ions are perturbed by the fact that they are located in an alloy host rather than in pure RbI. In particular, when RbReO₄ is used as a dopant in low concentrations, the satellite lines disappear.⁹

The doped alkali halide crystals were grown by Czochralski techniques with the [100] axis along the pulling direction. The alkali halide starting material was Merck Suprapur grade, which was purified by bubbling with a suitable halogen gas. The crystals were doped by addition of the appropriate dopant [KReO₄ or RbReO₄ (Ref. 19)] to the melt before pulling. To remove stress and impurity-concentration gradients, samples were annealed under argon at temperatures within 30–50°C of the melting point for 2 h.

III. EXPERIMENTAL METHODS AND DATA ANALYSIS

The relaxation of a vibrationally excited molecule can be characterized by an energy relaxation time T_1 and a dephasing time T_2 (lifetime of the macroscopic polarization or coherence of the excited state). These lifetimes can be extracted from several linear and nonlinear spectroscopic measurements. For homogeneously broadened vibrational modes the measurements are straightforward, whereas inhomogeneously broadened systems require a more sophisticated approach. In the former case, T_2 may be extracted from linear spectroscopy with conventional spectrometers or diode lasers. T_1 may be obtained directly from incoherent laser saturation. In the latter case, T_2 can be obtained from transient hole-burning spectroscopy under the assumption that the measured hole width is simply related to the homogeneous linewidth. Then, incoherent saturation can be used to extract values for the $T_1 T_2$ product, from which values for T_1 can be deduced.

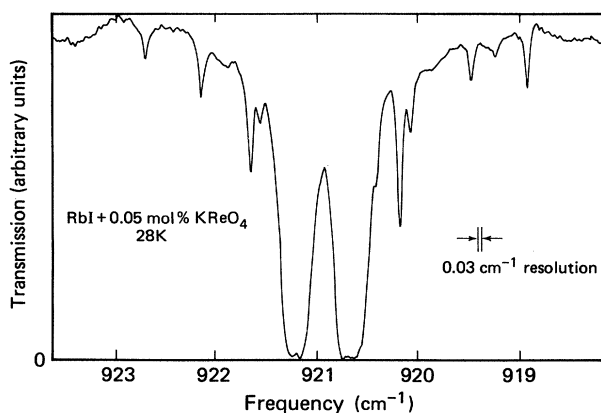


FIG. 4. High-resolution transmission spectrum of RbI + 0.05 mol % KReO₄ at 28 K. Sample length, 0.172 cm.

This section describes these two methods in more detail.

For temperatures between 1.4 and 300 K samples were mounted in a variable-temperature pumped-liquid-helium optical cryostat or in a closed-cycle refrigerator. Sample temperatures were measured with calibrated carbon resistors. For high-temperature measurements the sample was mounted in a variable-temperature brass cavity. A thermocouple embedded in the face of the sample recorded the sample temperature.

A. Determination of T_2 : Hole-burning

The dephasing time T_2 in homogeneously broadened systems is related to the absorption linewidth $\Delta\nu$ (FWHM) by $T_2 = (\pi \Delta\nu)^{-1}$. In inhomogeneously broadened systems the homogeneous linewidths are masked by the broader inhomogeneous width. The technique of hole-burning spectroscopy allows measurement of the homogeneous linewidth inside an inhomogeneously broadened absorption line under the assumption of no spectral diffusion. Since the measured hole widths were independent of ReO₄⁻ concentration, this assumption is valid. A pump laser at ν_0 partially saturates absorbers with center frequency near ν_0 , and a tunable low-power probe laser measures the frequency-dependent decrease in absorption (Fig. 5). The homogeneous linewidth and T_2 can be extracted from the hole line shape. It can be shown that at laser intensities well below I_s the hole width $\Delta\nu_H$ is twice the homogeneous width,^{20,21} yielding $T_2 = (2/\pi \Delta\nu_H)^{-1}$.

High-resolution spectra of very narrow linewidths were obtained with a diode-laser spectrometer shown in Fig. 6. A Pb_{0.86}Sn_{0.14}Te diode laser cooled in a closed-cycle refrigerator provided tunable radiation near 10.8 μm . The mechanically chopped laser radiation was directed through the sample and a monochromator for mode selection. The light was then split by a beam splitter. Part of the beam was detected by a cooled HgCdTe detector and a lock-in amplifier. The other part of the beam passed through a 2.54-cm Ge étalon which provided relative frequency markers spaced by 0.049 18 cm⁻¹. Absolute frequencies were determined by observing the $P(42)$ absorption line of the (00^o1)-(10^o0) transition in hot CO₂ gas. Ex-

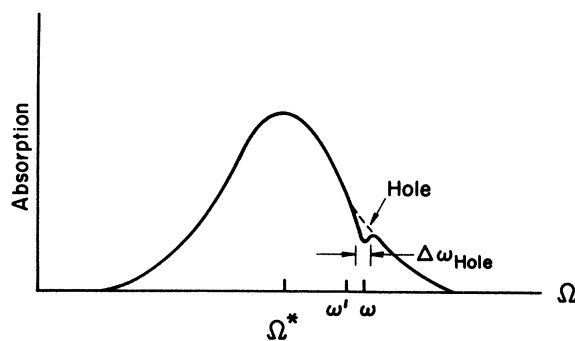


FIG. 5. Hole burning in an inhomogeneously broadened absorption line. ω is the fixed pump frequency, ω' is the variable probe frequency, and Ω^* is the center of the distribution of transition frequencies Ω .

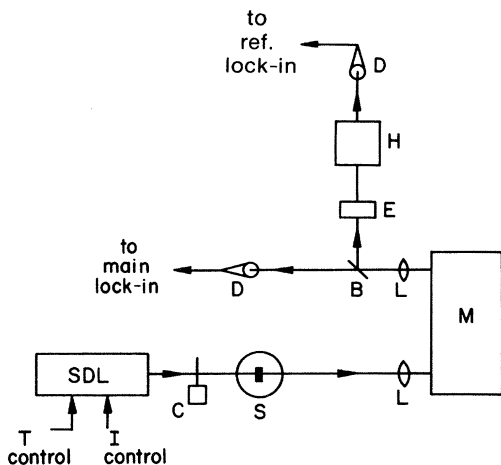


FIG. 6. Experimental arrangement for high-resolution spectroscopy with the diode laser. *B*, beamsplitter; *C*, chopper; *D*, 77-K HgCdTe detectors; *E*, 2.54-cm Ge étalon; *H*, hot CO₂ cell; *L*, lens; *M*, 0.75-m monochromator; *S*, sample in a cryostat or closed-cycle refrigerator; *SDL*, semiconductor diode laser.

amples of high-resolution spectra of the ν_3 absorption of ReO_4^- can be found in Refs. 6 and 13.

The experimental arrangement for diode-laser-CO₂-laser hole-burning spectroscopy is shown in Fig. 7. A longitudinally excited CO₂ laser was used as the saturating pump. Several high-*J* lines from the 10- μm *P* branch were utilized depending upon the host crystal. Because the high-*J* lines have relatively low gain, only one longitudinal mode was observed to lase for almost all operating conditions. The frequency jitter of the laser was approximately 2 MHz due to plasma-density fluctuations and variations in cavity length.

The pump beam was focused on the sample and was attenuated with calibrated CaF₂ attenuators. The pump-beam polarization was rotated into the horizontal plane with a zero-order wave plate. The vertically polarized probe beam was generated by a current- and temperature-tunable $\text{Pb}_{0.86}\text{Sn}_{0.14}\text{Te}$ semiconductor diode laser. A 0.75-m monochromator was used to reject unwanted longitudinal modes. After passage through the cooled sam-

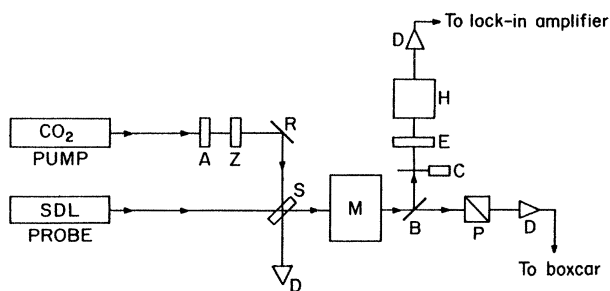


FIG. 7. Experimental arrangement for diode-laser-CO₂-laser hole-burning spectroscopy. *A*, CaF₂ variable attenuators; *B*, beam splitter; *C*, chopper; *D*, detector; *E*, Ge étalon; *H*, hot CO₂ cell; *M*, monochromator; *P*, polarization analyzer; *R*, mirror; *S*, sample in variable-temperature helium Dewar; *Z*, zero-order $\lambda/2$ waveplate; *SDL*, semiconductor-diode laser.

ple and the monochromator, the probe beam was split into two beams. After rejection of scattered pump light with a polarizer the main probe beam was detected with a 77-K HgCdTe detector and a boxcar integrator. The second probe beam was chopped and sent through a hot CO₂ cell at 300°C before it was focused on a second HgCdTe detector. This chopped diode-laser signal was detected with a lock-in amplifier.

The hole signal was detected using a zero-background technique. The pump was pulsed at approximately 23 Hz with a duty cycle of 4.5×10^{-3} (0.2-msec pulse width). The probe beam was continuous wave, and the pulsing pump produced synchronous increases in the sample transmission. The boxcar was adjusted to measure the peak of the changing probe signal (boxcar aperture 60 μsec , 100- μsec plug-in time constant). This detection technique produced zero background signal when the probe frequency was not coincident with $P(42)$, the frequency of the hole. Absolute and relative probe frequencies were determined by observing the $P(42)$ absorption in the hot-CO₂-gas cell and the transmission fringes from a 2.54-cm Ge étalon, respectively. The diode-laser frequency jitter was roughly 10 MHz, and the tuning rate was 6.2 $\text{cm}^{-1}/\text{\AA}$.

The hole spectra, hot-CO₂-gas absorption spectra, and étalon fringes were acquired with a desktop calculator. For the measurements of the low-power hole width, the pump intensities were experimentally maintained below levels that produced appreciable power broadening.

The diode-laser-CO₂-laser hole-burning measurements were limited to linewidths greater than 10 MHz (the stability of the diode laser). Higher-resolution measurements required a CO₂ probe laser in place of the diode laser. Figure 8 shows the experimental setup for CO₂-laser-CO₂-laser hole burning. A commercial, longitudinally excited CO₂ laser was used as the vertically polarized tunable probe. Tunability was achieved by varying the cavity length with a piezoelectric transducer mount for the output mirror. The probe laser was operated in the continuous-wave mode in order to achieve optimum frequency stability. No active cavity-length or cavity-temperature stabilization was used for these experiments. Following the probe path in Fig. 8, the average power was monitored with a power meter. A portion of the probe beam was split off and sent to the heterodyne beat detector. Calibrated CaF₂ attenuators at position *A_B* were used to adjust the probe intensity at the sample. A ZnSe lens focused the probe beam on the sample, yielding a spot radius of 0.035 cm at the $1/e^2$ points. A second lens positioned behind the cryostat recollimated the probe beam, and more CaF₂ attenuators at position *A_C* allowed the signal at the detector to be adjusted. A stack-of-plates polarizer was used to reject horizontally polarized, scattered pump radiation. Just in front of the detector, a narrow-band ir filter (10.6–11.3 μm) was used to reject black-body noise from the laser discharge itself. This filter was essential at low power levels, because with 30 mm of CaF₂ in the probe beam, the broad-band black-body signal from the laser discharge was larger than the 10.8- μm ir signal. Finally, an extremely sensitive liquid-He-cooled Si:As detector was used to measure the hole-burning signal.

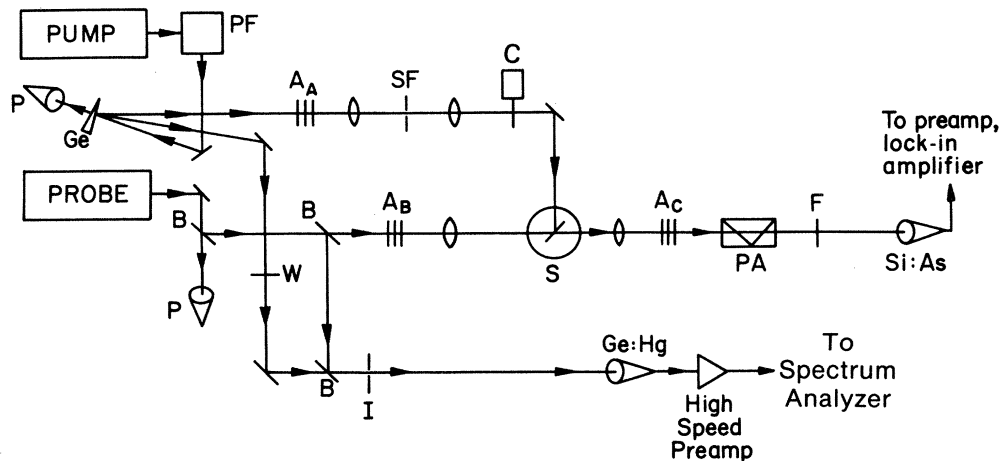


FIG. 8. Experimental arrangement for CO₂-laser-CO₂-laser hole-burning spectroscopy. Legend: A_A, A_B, A_C , CaF₂ attenuators; C, chopper; F, narrow-band filter (10.6–11.35 μm); Ge, uncoated Ge wedge; Ge:Hg, ultrahigh-speed Ge:Hg detector; I, iris; P, average power meter; PA, polarization analyzer; PF, two-mirror polarization flipper; S, sample in cryostat; SF, 0.011-in. spatial filter; Si:As, Si:As detector; W, zero-order $\lambda/2$ waveplate. The pump and probe lasers are longitudinally excited CO₂ lasers with piezoelectric cavity length and grating tuning.

A second longitudinally excited CO₂ laser was used to generate the saturating pump beam. Of course, the pump and probe lasers were always operated on the same laser line. The exact frequency of the pump laser could be fine-tuned using a piezoelectric transducer on the output mirror. The pump frequency was usually adjusted to lie at the center of the probe-laser tuning curve. The pump laser was operated in the cw mode in order to achieve maximum frequency stability. No active stabilization was used, however.

Following the pump beam path in Fig. 8, the vertically polarized beam exiting from the laser was sent through a two-mirror polarization flipper to produce horizontally polarized radiation. Using a wedged Ge beamsplitter, the beam was split into a beam for sample saturation and a beam for heterodyne frequency calibration. The polarization of the latter beam was rotated back to the vertical using a zero-order $\lambda/2$ waveplate. This beam was overlapped in space with a vertically polarized beam from the probe and was sent to the Ge:Hg heterodyne beat detector.

The main pump was attenuated by CaF₂ flats at position A_A and then was carefully spatially filtered through a 0.011-in.-diam pinhole. The resulting spot on the sample was Gaussian in transverse distribution with a beam radius at the $1/e^2$ points of 0.073 cm. The spatially filtered and attenuated pump beam was mechanically chopped with a 50% duty cycle. The pump intensities were maintained in the range 0.5–5 W/cm², which produced no observable power broadening of the holes. The resulting hole heights were typically $\Delta T/T_i \leq 0.04$, where T_i is the initial sample transmission. The overlap region of the pump and probe beams had the desirable characteristic of having the probe spot smaller than the pump spot. This produced good efficiency in the generation of the hole signal because all portions of the probe beam experienced the transmission change caused by the pump.

The probe frequency was calibrated by overlapping the

beams from each of the two lasers on a Ge:Hg ultrahigh-speed liquid-He-cooled photoconductive detector and measuring the beat frequency. The detector signal was preamplified, and the resulting beat signal was displayed on a precision spectrum analyzer. The peak-to-peak jitter in the beat note between the two lasers was (2.5 ± 0.5) MHz for a 3-sec averaging time. For very short observation times, the emission linewidth of each laser would be much smaller—roughly 30 kHz. However, the center frequencies of the two lasers jittered rapidly on the time scale of milliseconds, due to discharge-index-of-refraction and cavity-length fluctuations. Thus, the effective resolution of these hole-burning measurements was 2.5 MHz, a factor of 4 better than that achieved in the diode-laser-CO₂-laser hole-burning experiments.

Holes were observed using a zero-background technique similar to that described earlier. The chopped pump beam produced synchronous changes in the cw probe-beam transmission. The resulting time-varying signal from the Si:As detector was preamplified and analyzed with a vector lock-in amplifier. As the probe frequency was slowly scanned across the hole, the output of the lock-in amplifier was recorded on an x - y recorder. Figure 9 illustrates a typical hole spectrum recorded using this technique.

B. Determination of T_1 or $T_1 T_2$: Incoherent saturation

Incoherent laser-saturation measurements provide a measure of the excited-state lifetime T_1 for homogeneously broadened systems and the product $T_1 T_2$ for inhomogeneously broadened systems. In this technique the intensity-dependent transmission of a sample is measured for pulse widths much longer than T_1 and T_2 . The laser intensity at position z follows the usual relation²²

$$\frac{dI(z)}{dz} = \frac{-\alpha_0 I(z)}{[1 + I(z)/I_s]^b} - \alpha_n I(z), \quad (1)$$

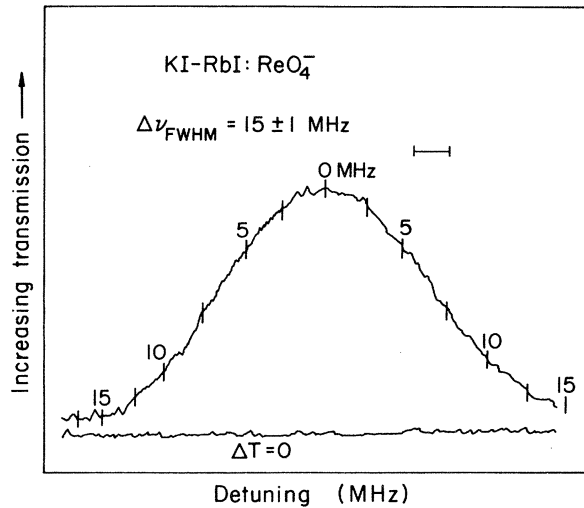


FIG. 9. Fully normalized and calibrated hole spectrum for KI + 0.05 mol % KReO_4 + 2.5 mol % RbI at 1.4 K. The $\Delta T = 0$ line corresponds to the signal level with either the pump or the probe blocked. The pump intensity at the sample is 3.3 W/cm^2 and the probe intensity is 0.35 W/cm^2 .

where α_n is the nonsaturable loss coefficient,²³ α_0 is the (saturable) loss coefficient measured at low intensities, $b = 1$ for homogeneously broadened absorptions and $b = \frac{1}{2}$ for inhomogeneously broadened absorptions, and I_s is the saturation intensity. For homogeneously broadened systems,

$$I_s = \hbar\Omega / 2T_1\sigma, \quad (2)$$

where Ω is the laser frequency and σ is the absorption cross section. For inhomogeneously broadened absorptions,

$$I_s = \frac{\eta c \hbar^2}{8\pi T_1 T_2 L |\vec{\mu}|^2 / 3}, \quad (3)$$

where η is the refractive index, $|\vec{\mu}|$ is the dipole moment, and $L = [\frac{1}{3}(\eta^2 + 2)]^2$ is the local-field correction. This expression can be simplified by using the sum rules

of Appendix A to substitute for the dipole moments and local-field factors to yield

$$T_1 T_2 = \frac{N}{4cSI_s} \hbar\Omega_3, \quad (4)$$

where N and S are the density of ReO_4^- molecules and the integrated absorption strength for that density, respectively. Since the dipole moment is independent of host, the ratio N/S is as well; hence this ratio need only be measured for one host. Equation (4) illustrates the important fact that the $T_1 T_2$ product can be obtained from the saturation intensity without the necessity of calculating the local-field factors.

Equation (1) can be integrated as shown in Appendix B to yield implicit relations between the sample transmittance and the incident-laser intensity, with two parameters I_s and α_n . A nonlinear least-squares-fitting procedure can then be used to extract values for these two parameters.

Measurements of the intensity-dependent sample transmission were performed using the experimental apparatus shown in Fig. 10. The beam from a longitudinally excited line-tunable CO_2 laser was monitored by average-power and peak-power detectors. Before impinging on the cryostat, the laser beam was attenuated with calibrated CaF_2 flats and spatially filtered using a telescope with a pinhole at the focus. The second lens of the telescope was adjusted to focus the beam on the sample. The sample was mounted in a variable-temperature cryostat. The beam transmitted through the cryostat was recollimated before passing through a second set of CaF_2 attenuators. A $10.8\text{-}\mu\text{m}$ narrow-band filter passing $10.6\text{--}11.35 \mu\text{m}$ was used to reject any spurious black-body radiation from the laser discharge. Finally, the infrared beam was focused on a helium-cooled Ge:Cu detector.

The CO_2 laser was typically pulsed at a 1% duty cycle for these measurements. The pulse width was approximately 0.10 msec. Average power levels at the sample were maintained below the onset of heating, as determined by the resistance of a 1-k Ω carbon resistor mounted directly on the sample. The Ge:Cu photoconductive detector signal was preamplified and filtered with a bandpass of 30 Hz to 300 kHz. The peak amplitude of the laser pulse was detected using one channel of a boxcar

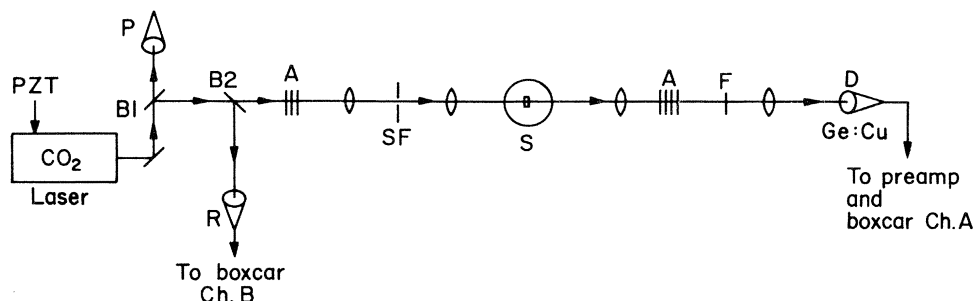


FIG. 10. Typical experimental apparatus for laser saturation measurements. Legend: A, CaF_2 calibrated attenuators; B1 and B2, beamsplitters; D, Ge:Cu detector; F, $10.8\text{-}\mu\text{m}$ narrow-bandpass filter; P, average power detector; PZT, piezoelectric transducer for cavity-length adjustment; R, pyroelectric reference pulse detector; S, sample cryostat; SF, 0.011-in.-diam spatial filter.

integrator. Channel 2 of the boxcar was used to monitor the peak power at the reference pulse detector. The boxcar aperture was 30 μ sec, and the integrating time constant was 1 msec. Sample transmission as a function of incident-laser intensity was measured by moving the calibrated attenuators one by one from the input side of the cryostat to the output side. This method kept the signal at the detector fairly constant and thus avoided errors due to detector nonlinearity.

A typical example of the incoherent saturation measurements is shown in Fig. 11. The figure shows the sample transmission as a function of the incident intensity for KI-RbI:ReO₄⁻ at 1.4 K. The solid line shows a fit to the data using the equations of Appendix B, from which values for I_s and α_n have been extracted. It is important to realize that Eq. (1) assumes uniform intensity across the laser spot. Since Gaussian-profile laser beams were used for these experiments, the measured raw sample transmittances were corrected by utilizing the exact decomposition of a Gaussian-averaged nonlinear function presented by Kolodner *et al.*²⁴

IV. RESULTS

Temperature-dependent linear spectroscopy allows several general conclusions to be made regarding the ν_3 mode of ReO₄⁻ molecules in alkali halides. For all pure hosts except heavily doped RbI, the ν_3 mode appears as a single narrow line with a low-temperature width of ~ 0.02 cm⁻¹. The absence of a strong phonon sum band on the ReO₄⁻ zero-phonon line at low temperatures indicates that the molecular vibration is only weakly coupled to the lattice. Furthermore, the absence of librational sidebands in almost all hosts indicate that librational motion of the large ReO₄⁻ molecule is essentially quenched. This is to

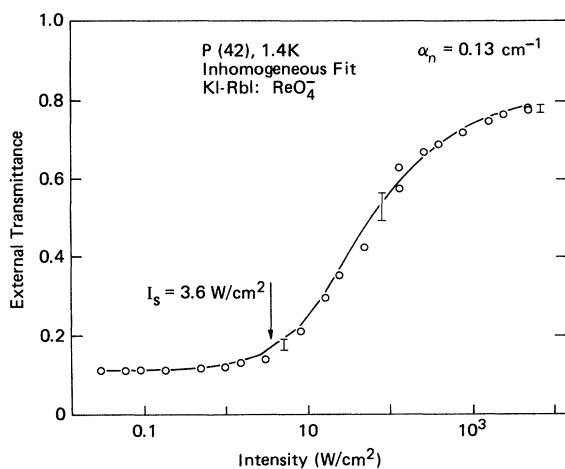


FIG. 11. External transmittance versus peak incident intensity for KI-RbI:ReO₄⁻ at 1.4 K. The Gaussian-averaged nonlinear function correction has been applied to raw transmittances in order to generate the plotted values. The solid line is a fit to the data using the inhomogeneous broadening model.

be contrasted with CN⁻ in alkali halides, for example, in which a clear librational sum band is observed at low temperatures.²⁵ Moreover, anharmonicity of the ReO₄⁻ mode prevents the frequency of the first overtone, $2\nu_3$ (1841 cm⁻¹ in KI),¹⁷ from equaling twice the fundamental (922.5 cm⁻¹ in KI at 77 K).¹⁷ This means that ladder transitions are not possible. Thus the ReO₄⁻ ν_3 vibrational mode can be reasonably approximated by an isolated two-level system. Alloying of pure hosts with a small amount of Rb⁺ ions produces smooth, inhomogeneously broadened lines up to 2 cm⁻¹ wide. On the other hand, alloying with a small amount of Cs⁺ ions⁶ weakly splits the main ν_3 mode absorption, producing a number of narrow (~ 0.02 cm⁻¹ wide) lines as far as 0.2–0.4 cm⁻¹ from line center. As pointed out earlier, these broadenings and splittings are responsible for the CO₂-laser–line coincidences in these systems.

Figure 12 (open circles) shows the complete temperature dependence of the linewidth of the ReO₄⁻ ν_3 mode in pure KI, as determined by linear spectroscopic techniques. Various samples with nominal concentrations of ReO₄⁻ molecules between 0.001 and 0.005 mol % were measured in these experiments. The line shape is Lorentzian above 30 K, indicating that the transition is homogeneously broadened. Below 30 K the line shape is Gaussian, indicating that the measured linewidth no longer represents the homogeneous width. In this temperature range the homogeneous linewidth was measured by hole-burning spectroscopy.

Figure 12 (solid symbols) also shows hole-burning measurements of the homogeneous linewidth of the ReO₄⁻ ν_3 mode for $T < 25$ K. This is a clear demonstration of the ability of the hole-burning technique to measure homogeneous widths inside a broader inhomogeneous line. The solid squares represent the hole-burning results for the KI-RbI alloy host; the triangles represent equivalent data for the KI-CsI host. Hole-burning experiments were limited to temperatures below 25 K due to the rapid increase of I_s and consequent decrease in hole depth with increasing temperature. Note that the data for the pure KI and the alloy hosts connect continuously at 25 K. Further, the homogeneous linewidths are essentially equal for the two alloy hosts, despite the large difference in inhomogeneous widths. This indicates that the hole widths are determined by some intrinsic parameter of the KI host lattice, e.g., phonons, rather than by the nature of the second dopant. The double-doping procedure has the useful property of producing a coincidence with the P(42) CO₂-laser line, yet has a negligible effect on the homogeneous linewidth of the ReO₄⁻ ν_3 mode. Before analyzing the linewidth results it should be pointed out that the hole width grew roughly as \sqrt{I} ,¹³ as theoretically expected,²⁶ and was independent of ReO₄⁻ concentration. Recent studies on the validity of the Bloch equations²⁷ indicate that the hole width should grow more slowly than \sqrt{I} . There is a suggestion of this trend in our data,¹³ but the signal-to-noise ratio is insufficient to provide a strong confirmation.

There are two classes of phonon-interaction phenomena²⁸ that may affect the low-power linewidth of the ν_3 -mode absorption of ReO₄⁻ molecules in alkali halides:

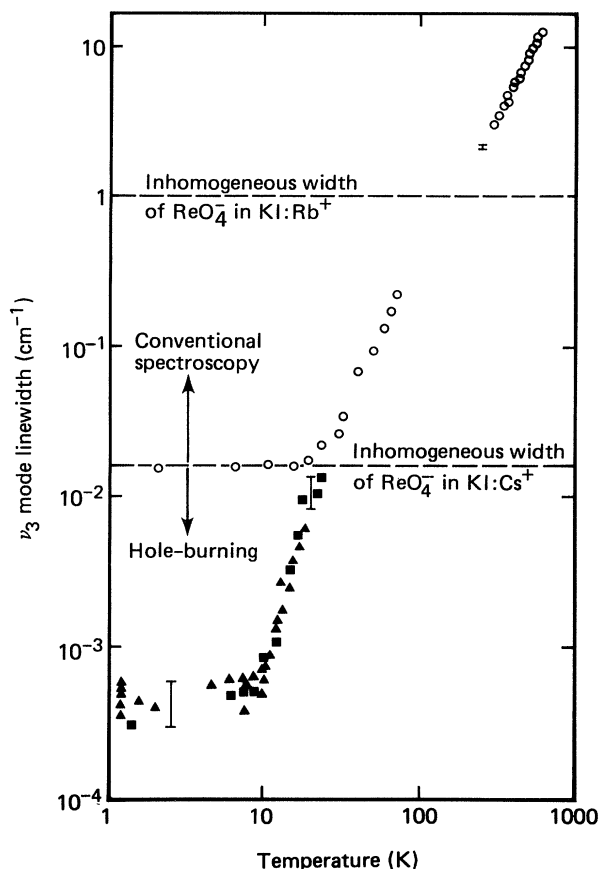


FIG. 12. Linewidth (FWHM) of the ν_3 vibration of ReO_4^- in KI crystals versus temperature. The open circles represent linear spectroscopic measurements. The solid squares represent hole-burning results for samples of composition KI + 0.005 mol % KReO_4 + 2.5 mol % RbI, and the solid triangles represent equivalent data for KI + 0.05-mol % KReO_4 + 0.2-mol % CsI samples. The inhomogeneous linewidths for these two hosts are indicated.

decomposition and scattering processes. The phonon decomposition mechanism consists of an energy-conserving decay of the vibrational mode into a large number of lattice phonons, the number of phonons being determined by the vibrational-mode frequency and the highest available phonon frequency. This is actually a T_1 process, and when $T_2 \ll T_1$ it does not affect the homogeneous linewidth of the ν_3 -mode absorption. However, if the internal mode is lifetime-broadened ($T_2 \sim T_1$), this process can affect the temperature dependence of the linewidth. The phonon scattering process, on the other hand, involves the elastic interaction of lattice phonons with the vibrational mode. This is a T_2 process, in which the phase of the vibrational mode is interrupted by a collision with a phonon.

Both types of interactions have predictable temperature dependences which can be compared to the measured values to determine which, if either, process contributes to the observed linewidths. In decomposition processes, energy-conservation considerations determine the minimum number n of phonons into which a vibrational exci-

tation can decay (for KI, $n=7$). It has been shown²⁸ that at low temperatures ($T \ll \Theta_D$) the linewidth is independent of temperature, whereas at high temperatures the linewidth varies as T^{n-1} . Thus the predicted temperature dependence for ReO_4^- in KI at high temperatures is T^6 . The high-temperature slope in Fig. 12 is 2.08 ± 0.15 . Therefore we conclude that the decomposition process is not responsible for the observed temperature dependence.

The temperature-dependent linewidth arising from the phonon scattering process assuming a Debye phonon spectrum is²⁹

$$\Delta\nu(T) - \Delta\nu(0) = \beta \left[\frac{T}{\Theta_c} \right]^7 \int_0^{\Theta_c/T} \frac{x^6 e^x}{(e^x - 1)^2} dx, \quad (5)$$

where β and Θ_c are parameters. The cutoff of the Debye spectrum Θ_c is a variable parameter because the model does not predict which phonons are most effective in scattering from the ν_3 vibration.

The data in Fig. 12 are replotted in Fig. 13 after subtracting the low-temperature linewidth $\Delta\nu(0)$. The solid

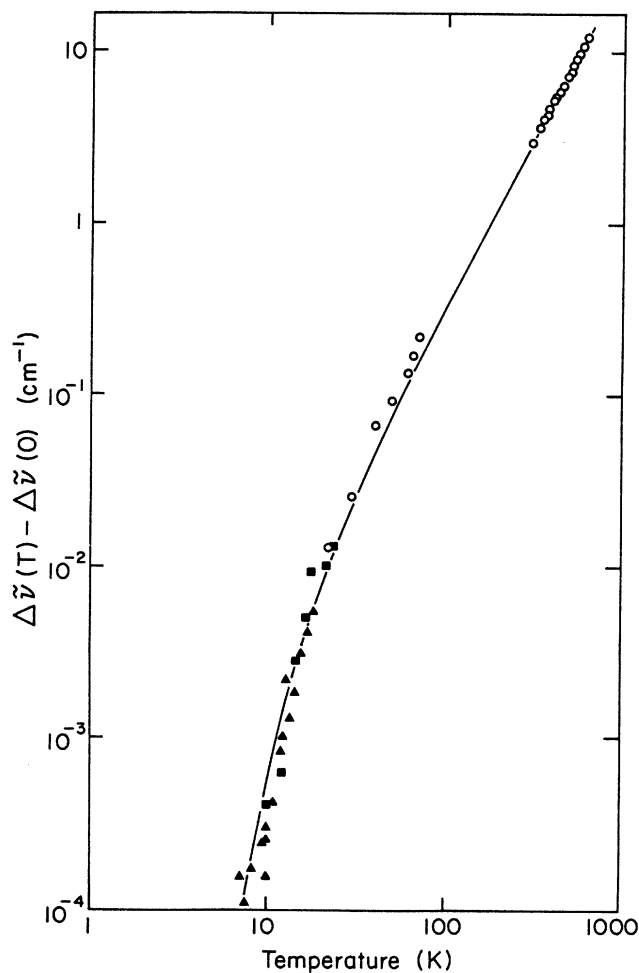


FIG. 13. Excess homogeneous linewidth $\Delta\nu(T) - \Delta\nu(0)$ versus temperature. The solid curve is the predicted temperature dependence for elastic scattering with $\Theta_c = 65$ K and $\beta = 0.70$ cm^{-1} [Eq. (5)]. Θ_c is the cutoff temperature for a Debye phonon spectrum, and β is an overall multiplicative fitting constant.

line is given by Eq. (5), which describes the complete temperature dependence of the linewidth for the phonon scattering model. The best-fit values of the fitting parameters are Debye-spectrum cutoff, $\Theta_c = (65 \pm 5)$ K, and overall multiplicative factor, $\beta = (0.7 \pm 0.10)$ cm⁻¹. The fit to the data is quite good, confirming that phonon scattering is the dominant dephasing mechanism above 10 K. The value of Θ_c corresponds to a maximum phonon frequency of 45 cm⁻¹, which correlates well with the dominant acoustic-phonon frequencies in KI.³⁰ That acoustic phonons scatter more strongly from the ReO₄⁻ molecule than do optic phonons can be understood from a cursory examination of the local lattice at the ReO₄⁻ site. The tetrahedral ReO₄⁻ molecule enters the lattice substitutionally with the Re—O bonds along body diagonals of the cubic lattice. Because the I⁻ ions are much larger than the K⁺ ions, the I⁻ ions are closer to the tetrahedral arms of the molecule than the K⁺ ions, even though the latter are nearest neighbors. In the region of a large density of phonon states, namely, the zone edges, the I⁻ ions oscillate with a large amplitude in the acoustic branches, while the K⁺ ions oscillate with a large amplitude in the optic branches. Therefore, it can be expected that the acoustic phonons in KI should interact more strongly with the molecule than do the optic phonons.

At temperatures below 10 K the homogeneous linewidth is temperature independent and consequently cannot be described by phonon scattering. To understand the low-temperature behavior of T_1 and T_2 , a systematic study of relaxation times as a function of host lattice is required. Table II summarizes the low-temperature relaxation times of ReO₄⁻ in various lattices. T_2 was computed from the homogeneous widths (as measured by hole-burning spectroscopy) using $T_2 = (\pi \Delta\nu_{\text{hom}})^{-1}$. Incoherent saturation studies yielded $T_1 T_2$ products, and from these values T_1 values were determined. Owing to the high saturation intensity and low absorption, respectively, hole-burning spectra could not be obtained for the NaI and KCl hosts.

Note that within experimental error, $T_2 \approx 2T_1$ for all hosts listed in Table II. It has been shown that if the dephasing of an excited state is dominated by excited-state decay, then $T_2 = 2T_1$.²⁰ Therefore, we conclude that

below 10 K the homogeneous linewidth of ReO₄⁻ is dominated by excited-state decay.

V. DISCUSSION AND CONCLUSIONS

One candidate for the decay mechanism is multiphonon, or n -phonon decay, as discussed earlier. In fact, the measured low-temperature linewidth (Fig. 12) is independent of temperature as expected for n -phonon decay processes. Multiphonon processes will now be considered in more detail.

The n -phonon decay rate W is expected to depend on lattice phonon frequencies according to³¹ $W \sim \exp(\gamma\nu_3/\nu_{\text{ph}})$, where γ is constant for a given alkali or halide series and ν_{ph} is a dominant phonon frequency. Recall that I_s is proportional to $(T_1 T_2)^{-1}$, but at low temperatures $T_2 \approx 2T_1$. Therefore I_s is proportional to T_1^{-2} . Since T_1^{-1} is a measure of W , a plot of $\log I_s$ versus ν_3/ν_{ph} should produce points that lie on various straight lines forming parallelograms, each line corresponding to a different alkali or halide series. Such a plot is shown in Fig. 14, in which the saturation intensity for various alkali halides is plotted versus the ratio of the ν_3 -mode frequency to the $\langle 100 \rangle$ LO-phonon frequency at the zone boundary. This abscissa variable can also be viewed as the number of phonons required to relax the ν_3 mode by n -phonon decay. The data for KBr, RbBr, KI, and RbI form reasonable parallelograms, but the data for NaI, RbCl, and KCl are anomalous. The dashed circles represent the approximate predicted values for these three hosts assuming the excited-state decay channel is the same as that for the other four hosts. The experimental values deviate from these predicted values by as much as 2 orders of magnitude. Further proof of the anomalous nature of the NaI, RbCl, and KCl decay rates is provided by plots of I_s versus lattice constant, bulk modulus, and longitudinal-acoustic-phonon frequencies.¹³ In all instances the experimental values for NaI are much higher than predicted, and the values for RbCl and KCl are much too low. If multiphonon decay is the relaxation mechanism for KBr, RbBr, KI, and RbI, a different excited-state decay process must be invoked for KCl, NaI, and RbCl.

TABLE II. Measured vibrational relaxation times for the ν_3 mode for ReO₄⁻ in alkali halide lattices ($T < 10$ K).

Host	RbI	KI	KI	KI	RbBr	KBr	RbCl	NaI	KCl
ReO ₄ ⁻ (mol %)	0.8	0.005	0.05	0.05	0.05	0.3	0.1	0.2	0.3
Other (mol %)	0.8 K ⁺	2.5 Rb ⁺	0.2 Cs ⁺	2 Na ⁺	0.05 K ⁺	2.5 Rb ⁺	0.1 K ⁺	0.2 K ⁺	2.2 Rb ⁺
$\bar{\nu}_3$ (cm ⁻¹)	922.9	922.9			927.0	931.0	933.0	938.7	939.0
	$P(42)$	$P(42)$			$P(38)$	$P(34)$	$P(32)$	$P(26)$	$P(26)$
Lattice constant a (Å)	7.34	7.07			6.85	6.60	6.58	6.47	6.29
I_s (W/cm ²)	0.9±0.2	3.6±0.8	6.8±1.4	3.2±0.6	14±3	53±10	9.3±2	> 700	22±5
α_n (cm ⁻¹) (±25%)	0.80	0.13	0.55	0.12	1.1	0.41	1.4		0.1
$T_1 T_2$ (10 ⁻¹⁶ sec ²)	24±5	6.7±1.5	3.6±0.8	7.6±1.5	1.8±0.4	0.49±0.09	2.9±0.6	< 0.05	1.2±0.3
$\Delta\nu_{\text{hom}}$ (MHz, FWHM)	5.0±1.5	7.8±0.5	9.0±1.3	10±1.5	18±1.5	30±1.5	17±1.3		
T_2 (10 ⁻⁸ sec)	6.4±2.0	4.1±0.3	3.5±0.5	3.2±0.5	1.8±0.2	1.1±0.1	1.9±0.2		
T_1 (10 ⁻⁸ sec)	3.8±1.4	1.6±0.5	1.0±0.3	2.4±0.5	1.0±0.3	0.45±0.15	1.5±0.3		

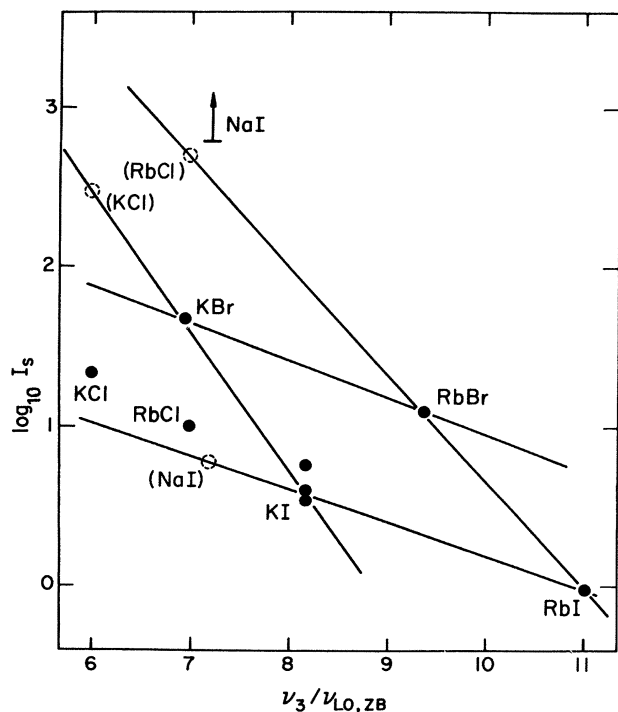


FIG. 14. Saturation intensity I_s versus ν_3 -mode frequency divided by the $\langle 100 \rangle$ LO-phonon frequency at the zone boundary (ZB), semilogarithmic plot. The solid lines are a guide to the eye. The solid circles represent measured values, and the symbol for NaI represents an estimated lower bound. The dashed circles signify expected values of I_s for NaI, KCl, and RbCl.

The small values of the measured relaxation times provide additional evidence that the multiphonon decay process might not be the correct description of the excited-state decay. The values of T_1 in Table II range between ~ 1 nsec for NaI and ~ 40 nsec for RbI. Using Gethins's

first-principles numerical calculation,¹ the excited-state relaxation time should be on the order of 100 msec, which dramatically contradicts the measured values.

To explain these large decay rates, a lower-order nonradiative decay process is needed. Analysis of the trends in Table II and Fig. 14 yields a process that involves a multistep emission of ReO_4^- internal modes, localized lattice modes around the ReO_4^- impurity, and band-phonon modes. This decay scheme is more complex in that the ν_3 mode emits a variety of vibrational excitations, but it is a more probable decay channel because it is of lower order. Before describing the process in detail, spectroscopic evidence for ν_3 coupling to internal and local modes will be discussed.

The linear transmission spectrum of $\text{RbI}:\text{ReO}_4^-$ (Fig. 1) shows combination lines, $(\nu_2 + \nu_3)$, $(\nu_4 + \nu_3)$, etc., that demonstrate anharmonic coupling between the ν_3 mode and other internal vibrational modes of the molecule. The $\nu_2(E)$ internal mode occurs at 337 cm^{-1} and the $\nu_4(T_2)$ mode appears at 335 cm^{-1} at low temperatures.

Furthermore, the Raman spectrum³² of $\text{KI}:\text{ReO}_4^-$ shown in Fig. 15 provides spectroscopic evidence that the ν_3 decay couples anharmonically to localized phonon modes of the lattice-defect system. Of special interest in this figure are the (local) modes of E_g and A_{1g} symmetry that appear above the cutoff of the optic-phonon branch. The $\nu_2(E)$ internal mode (solid line at 337 cm^{-1}) and the $\nu_4(T_2)$ internal mode (dashed line at 335 cm^{-1}) also appear in Raman scattering, as expected.

Figure 16 shows the local modes that result when a large substitutional impurity is added to a diatomic linear chain. These even modes are produced by the increase in the nearest-neighbor force constant at an anion site due to the substitution of the large ReO_4^- molecule for a halogen ion. The heavy ReO_4^- molecule is stationary and the nearest neighbors have large amplitudes in these modes.

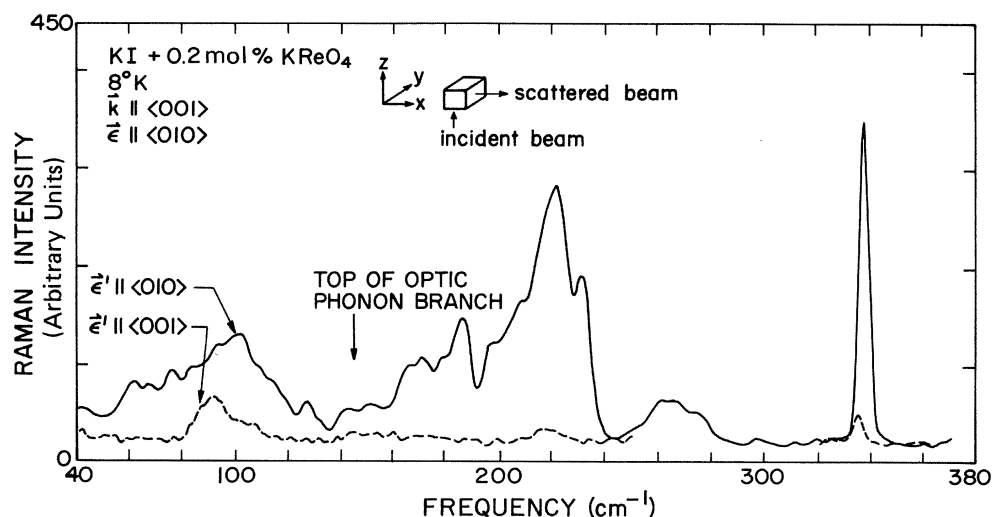


FIG. 15. Stokes Raman intensity versus frequency for $\text{KI} + 0.2 \text{ mol\% KReO}_4$ at 8 K . \vec{k} is the incident photon wave vector; \vec{e} and \vec{e}' are the incident and scattered polarization vectors, respectively. The spectrum represented by the solid line was taken with the analyzer parallel to the incident polarization. This configuration measures phonon modes of E_g and A_{1g} symmetry. The dashed spectrum was obtained with the analyzer perpendicular to the incident polarization in order to probe lattice modes of T_{2g} symmetry. The resolution is 3 cm^{-1} . The two-phonon-scattering spectrum of KI is weak and does not show in this figure.

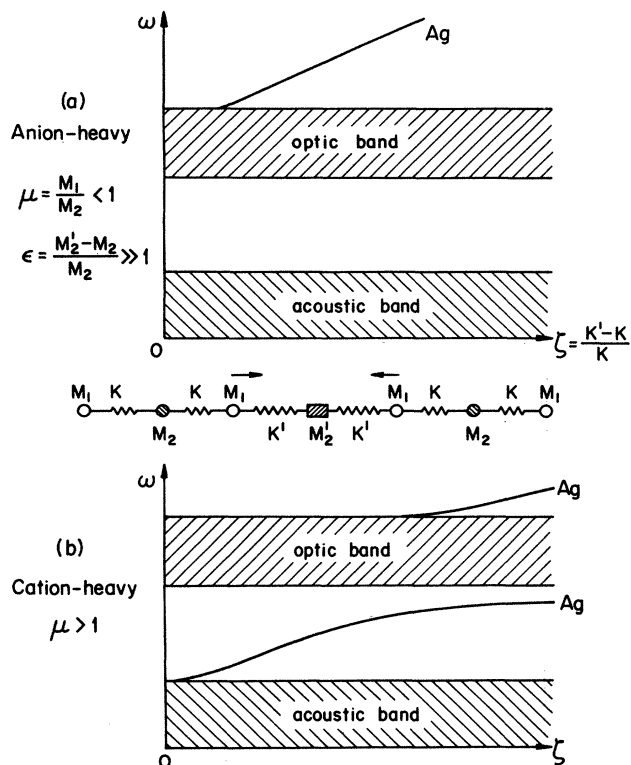


FIG. 16. Frequency of the A_g (even) local mode of a heavy substitutional impurity M_2' in a diatomic linear chain versus force-constant change ζ . (a) Anion-heavy case: $M_2 > M_1$. The even local mode appears at high frequencies above the optic-phonon frequency cutoff. (b) Cation-heavy case: $M_2 < M_1$. The local mode due to the impurity appears in the gap. At high values of force-constant change ζ , another even local mode slowly appears above the optic band.

Because of the lack of ReO_4^- motion, the actual value of the mass defect is unimportant. The even local mode observed above the optic-branch cutoff in KI (Fig. 15) is just the local mode that is rising out of the optic band for the anion-heavy host [Fig. 16(a)]. Even local modes should also rise out of the optic branch for other anion-heavy alkali halides with a gap (KBr and NaI). However, in cation-heavy RbCl, lower-frequency localized gap modes will rise out of the top of the acoustic spectrum [Fig. 16(b)], only to be accompanied by a higher-frequency local mode at large values of the force-constant defect.

Utilizing these internal modes of the ReO_4^- molecule and the localized modes of the lattice around the impurity, a lower-order decay scheme for the ν_3 mode can be devised. The following anharmonic process is the most probable decay channel: first, excitation of a pair of internal modes—either $2\nu_4$ (T_2) or $(\nu_2 + \nu_4)$ (T_2)—second, excitation of an even local mode, and last, the excitation of a small number of band phonons. The number of band phonons varies from alkali halide to alkali halide, and is determined by energy conservation. This model yields the correct qualitative behavior of I_s versus host lattice and should produce smaller predicted values for T_1 because fewer final-state vibrational excitations are required. It is

the changing energy of the localized phonon mode which accounts for the anomalous NaI, RbCl, and KCl data.

Figure 17 diagrams the expected ν_3 decay process for the various alkali halide hosts. In all cases, two lower-energy internal modes of the ReO_4^- molecule are excited. The remaining energy mismatch between ν_3 and $2\nu_4$ or $(\nu_2 + \nu_4)$ is provided by localized and extended phonon excitations. In KI, KBr, RbBr, and RbI, the energy mismatch is provided by the excitation of the even local mode and one band mode [Fig. 17(a)]. However, the extremely high value of I_s in NaI indicates that the local-mode frequency is sufficiently large to account for the mismatch by itself—no band phonons are required [Fig. 17(b)]. (The local mode in NaI occurs at a higher frequency than in the other hosts because it involves the motion of the lighter Na^+ ion.) In the RbCl case, the local mode occurs in the gap and is of much lower frequency, and hence two phonon modes are required to conserve energy [Fig. 17(c)]. Finally, for KCl [Fig. 17(d)], where the small value of the lattice constant leads to larger nearest-neighbor spring constants, the local mode is of

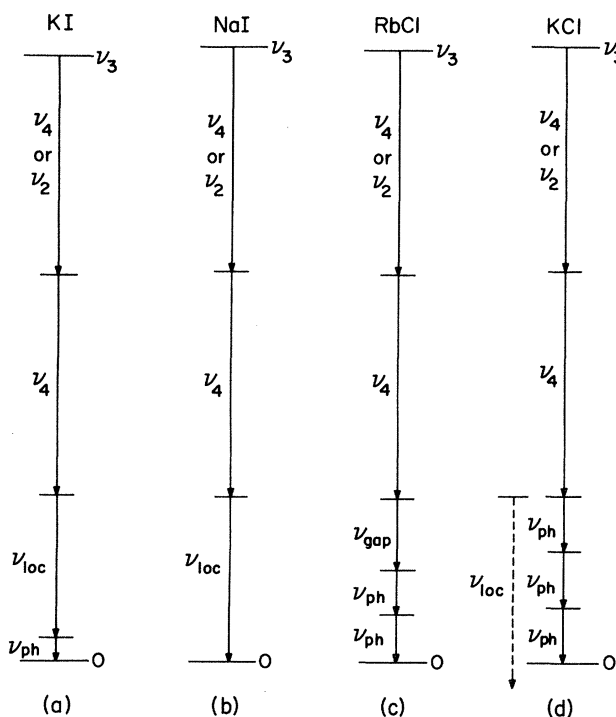


FIG. 17. Multistep anharmonic decay process for the ν_3 mode of ReO_4^- in alkali halides. (a) In KI, the energy of the ν_3 mode produces two internal mode excitations ($\nu_2 + \nu_4$) or $2\nu_4$, a local-mode excitation and a band phonon. (b) In NaI, the local-mode frequency has grown to the extent that no additional band phonon is required to achieve energy conservation. (c) In RbCl, the local mode occurs at lower frequency than in the other cases because it appears in the gap in the phonon spectrum. Hence, two band phonons are required to achieve energy conservation. (d) In KCl, the frequency of the local mode is so large that a local-mode excitation cannot be used to deexcite the ν_3 mode. Three band phonons are required to complete the decay.

such high frequency that it cannot participate in the decay process at all. Thus, the anomalies in I_s occur because the ν_3 -mode decay process is third order in NaI, fifth order in RbCl and KCl, and fourth order in all the other hosts.

The success of this multistep decay model in explaining the systematics of I_s is quite encouraging. The prominence of the even local mode in the various decay channels indicates that the ν_3 mode couples strongly to the motion of the nearest neighbors. This may explain why cation mixing of alkali halides has a much stronger effect on the ReO_4^- ir-absorption spectra than does anion mixing. The importance of the ν_2 and ν_4 internal modes of the molecule also has significant implications. A system in which the lowest internal modes occur at $10\ \mu\text{m}$ should have extremely long excited-state lifetimes. In this case, the fluorescence from such a system would be very strong, because the nonradiative decay time would be comparable to the spontaneous radiative decay time. To summarize, in the ReO_4^- system, the low-temperature excited-state decay times are controlled by a combination of internal, local, and band modes and not by the much slower multiphonon decay. An intrinsic upper limit to vibrational-mode relaxation times has not been observed. If a nonrotating spherical top molecule can be chosen properly so that the lowest-frequency internal mode is at least 6 or 7 times the highest lattice frequency, extremely large vibrational lifetimes should result, approaching the radiative lifetime.

It is instructive to compare the relaxation dynamics of ReO_4^- in alkali halides with vibrational relaxation mechanisms of molecules trapped in rare-gas matrices. A number of authors have investigated the vibrational relaxation of small polyatomic molecules trapped in rare-gas hosts. This expanding field has been reviewed by Dubost³³ and Legay.³⁴ The vibrational relaxation data for selected molecules in rare-gas matrices (RGM) are summarized in Table III. This table is not intended to be exhaustive; rather, it is designed to illustrate some of the relaxation mechanisms active in these systems. The longer relaxation times were measured by monitoring the fluorescence growth and decay following a laser-excitation pulse.

The faster relaxation rates were derived from the time-varying transmittance of a probe laser after an excitation pulse from a pump laser.

CO and NO in RGM (Refs. 33–36) have slow relaxation rates limited by spontaneous radiative decay. Because the excited state has a long lifetime, intermolecular vibrational energy transfer has been observed in these systems. The CO molecules cannot relax by rotating or emitting lower-energy vibrational excitations, and librational relaxation only serves to broaden the observed line shape.³⁶

NH_3 in N_2 (Ref. 37) and SF_6 in Xe (Ref. 38) have faster relaxation rates, probably because these systems can rotate and emit lower-frequency vibrational modes, respectively.

Of special interest are the recent results on the asymmetric tops CH_3F and CD_3F .^{39–41} The vibrational mode at $1036\ \text{cm}^{-1}$ in CH_3F is the lowest-frequency mode, yet the excited state relaxes quickly by the emission of many rotational quanta. In addition, the system has a permanent dipole moment, which allows intermolecular energy transfer to proceed via dipole-dipole coupling. The CD_3F ν_3 mode ($987\ \text{cm}^{-1}$) relaxes quickly to the lower-frequency ν_6 mode at $910\ \text{cm}^{-1}$ via phonon emission.

The ReO_4^- -alkali halide systems differ in two important respects from the molecules that have been isolated in rare-gas matrices. In all of the alkali halide lattices (with the exception of RbI, perhaps), the relatively large ReO_4^- molecule is prevented from rotating by steric effects. In addition, the molecule lacks a permanent dipole moment (also true for SF_6). These two characteristics imply that rotational relaxation is weak, and that vibrational diffusion via dipole-dipole interactions is small. However, the ν_3 -mode relaxation is still quite fast due to the availability of lower-frequency internal and local modes. It is clear that for a nonrotating spherical top molecule with the lowest vibrational mode near $10\ \mu\text{m}$, the excited-state decay rate could be very slow. In conclusion, our measurements on the ReO_4^- -alkali halide system and the previous studies of rare-gas-matrix-isolated molecules and U centers show that different combinations of impurity and host lattice can have quite different relaxation mechanisms. The vibrational relaxation dynamics in a

TABLE III. Summary of vibrational relaxation data for selected molecules in rare-gas matrices (some of the data in this table were selected from Ref. 33).

Molecule	Matrix	Vibrational Energy (cm^{-1})	Rotational Constant B (cm^{-1})	Relaxation Mechanism ^a	Relaxation Rate (sec^{-1})	References
CO	RGM, N_2	2140–1840	1.93	rad.,	50 in Ne	3
				inter. $V \rightarrow V$		
				$V \rightarrow L$		
NO	Ar, Ar + Kr	1870–1700	1.70	rad.		33
				inter. $V \rightarrow V$		
NH_3	N_2	970	9.94 ($A = 6.30$)	$V \rightarrow R$	6.6×10^4	37
SF_6	Xe	931		intra. $V \rightarrow V$	10^5	38
CH_3F	Kr	1036	0.85 ($A = 5.10$)	$V \rightarrow R$	9.1×10^4	39, 40
				inter. $V \rightarrow V$		
CD_3F	Kr	987	0.68 ($A = 2.55$)	intra. $V \rightarrow V$	9.1×10^3	40, 41

^aLegend: rad., radiative decay; inter. $V \rightarrow V$, intermolecular vibrational-vibrational transfer; $V \rightarrow L$, librational relaxation; $V \rightarrow R$, vibrational-rotational transfer; intra. $V \rightarrow V$, intramolecular vibrational-vibrational transfer.

particular case is determined by the details of the interaction between the vibrational mode and the other vibrational modes of the molecule and the host lattice.

ACKNOWLEDGMENTS

The authors gratefully acknowledge the use of diode lasers from General Motors Research Laboratories, the use of a CO₂ laser from Professor David Lee of Cornell University, and the use of an IR-98 Fourier-transform infrared spectrometer from IBM Instruments. This work has been supported in part by the U. S. Army Research Office under Grant No. DAAG-29-83-K-0044, by the National Science Foundation under Grant No. DMR-80-08546, by the National Science Foundation under Grant No. DMR-79-24008 through the Cornell Materials Science Center, and by the Office of Naval Research. The experimental data reported in this article were taken while one of the authors (W.E.M.) was located at Cornell University and while another author (A.R.C.) was located at General Motors Research Laboratories.

APPENDIX A: DIPOLE MOMENT FOR THE ReO₄⁻ ν₃ MODE

The integrated absorption sum rule provides a convenient method for measuring the dipole moment of the ν₃ vibrational mode. The sum rule can be written⁴²

$$\int_{\text{band}} \alpha(\tilde{\nu}) d\nu = \frac{\pi e^2}{\eta c^2 M^*} \left[\frac{\eta^2 + 2}{3} \right]^2 N f, \quad (\text{A1})$$

where $\tilde{\nu}$ is the frequency in wave numbers (cm⁻¹), η is the index of refraction, M^* is the effective mass, N is the density of oscillators per cm³, and f is the oscillator strength for the transition. f can be expressed in terms of the dipole moment using⁴³⁻⁴⁵

$$f = \frac{8\pi^2 M^* c \tilde{\nu}}{h e^2} \frac{|\vec{\mu}|^2}{3}, \quad (\text{A2})$$

which yields the expression

$$S = \int_{\text{band}} \alpha(\tilde{\nu}) d\tilde{\nu} = \frac{8\pi^3 \tilde{\nu}}{c h} \frac{L}{\eta} \frac{|\vec{\mu}|^2}{3} N, \quad (\text{A3})$$

where the local field correction factor is $L = [\frac{1}{3}(\eta^2 + 2)]^2$. Thus, in order to measure the dipole moment, the density of absorbers N and the integrated absorption strength S must be independently determined.

Four independent neutron-activation measurements of N were performed on samples of KI:ReO₄⁻. The total integrated absorption for each of the samples was measured at room temperature using a conventional infrared spectrometer, including corrections for reflection losses. The resulting value for the dipole moment of the ν₃ mode was computed to be $|\vec{\mu}| = 3.35(\pm 0.17) \times 10^{-19}$ esu cm, which implies an oscillator strength of $f = 1.3$ and an effective charge of $e^*/e = 1.14$.

APPENDIX B: EXTRACTION OF I_s FROM $T(I)$

Equation (1) can be integrated from $z=0$ to $z=L$, the sample length, to yield, for the homogeneous broadening case,

$$-(\alpha_0 + \alpha_n) = \ln \left[\frac{I(L)}{I(0)} \right] + \frac{\alpha_0}{\alpha_n} \ln \left\{ \left[\alpha_0 + \alpha_n \left(1 + \frac{I(L)}{I_s} \right) \right] / \left[\alpha_0 + \alpha_n \left(1 + \frac{I(0)}{I_s} \right) \right] \right\}. \quad (\text{B1})$$

For inhomogeneous broadening, integration of Eq. (1) gives

$$-\alpha_0 \left[1 - \left(\frac{\alpha_n}{\alpha_0} \right)^2 \right] L = \ln \left\{ \frac{(1 + I/I_s)^{1/2} - 1}{(1 + I/I_s)^{1/2} + 1} - \frac{\alpha_n}{\alpha_0} \ln \left[\frac{I}{I_s} \right] + 2 \frac{\alpha_0}{\alpha_n} \ln \left[1 + \frac{\alpha_n}{\alpha_0} \left(1 + \frac{I}{I_s} \right)^{1/2} \right] \right\} \Bigg|_{I(0)}^{I(L)}. \quad (\text{B2})$$

Both of these equations are implicit, nonlinear relations between $I(L)$ and $I(0)$ with parameters I_s and α_n . Given values for the parameters and $I(0)$, a predicted value for $I(L)$ can be computed using the modified secant iteration procedure.⁴⁶

The experimental measurements yield actual values for $I(L)$ for each value of $I(0)$. Marquardt's technique^{47,48} was used to determine best fit values of I_s and α_n using as a criterion the minimization of the sum of squares of the deviations between predicted and actual values for $I(L)$.

¹T. Gethins, Can. J. Phys. **48**, 580 (1970).

²H. Dubost, L. Abouaf-Marguin, and F. Legay, Phys. Rev. Lett. **29**, 145 (1972).

³H. Dubost and R. Charneau, Chem. Phys. **12**, 407 (1976).

⁴L. C. Lee and W. L. Faust, Phys. Rev. Lett. **26**, 648 (1971).

⁵A. R. Chraplyvy and A. J. Sievers, Opt. Lett. **3**, 112 (1978).

⁶A. R. Chraplyvy, W. E. Moerner, and A. J. Sievers, Opt. Lett. **6**, 254 (1981).

⁷A. R. Chraplyvy, W. E. Moerner, and A. J. Sievers, Opt. Lett. **6**, 431 (1981).

⁸W. E. Moerner, A. J. Sievers, and A. R. Chraplyvy, Phys. Rev. Lett. **47**, 1082 (1981).

⁹W. E. Moerner, A. J. Sievers, R. H. Silsbee, A. R. Chraplyvy, and D. R. Lambert, Phys. Rev. Lett. **49**, 398 (1982); W. E. Moerner, A. R. Chraplyvy, A. J. Sievers, and R. H. Silsbee, Phys. Rev. B **28**, 7244 (1983).

- ¹⁰Y. Yang and F. Lüty, *Phys. Rev. Lett.* **51**, 419 (1983).
- ¹¹H. Bilz and W. Kress, *Phonon Dispersion Relations in Insulators* (Springer, Berlin, 1979).
- ¹²*American Institute of Physics Handbook*, 3rd ed., edited by Dwight E. Gray (McGraw-Hill, New York, 1972).
- ¹³W. E. Moerner, Ph.D. thesis, Cornell University, 1981; Cornell Materials Science Center Report No. 4588 (unpublished).
- ¹⁴R. S. McDowell, L. J. Radzienski, H. Flicker, H. W. Galbraith, R. C. Kennedy, N. G. Nereson, B. J. Krohn, J. P. Aldridge, J. D. King, and K. Fox, *J. Chem. Phys.* **69**, 1513 (1978).
- ¹⁵Y. J. Chabal, Ph.D. thesis, Cornell University, 1980.
- ¹⁶H. H. Claassen and A. J. Zielen, *J. Chem. Phys.* **22**, 707 (1954).
- ¹⁷M. R. Mohammad and W. F. Sherman, *J. Phys. C* **14**, 283 (1981).
- ¹⁸This spectrum was taken with an IBM Instruments IR-98 Fourier-transform infrared spectrometer.
- ¹⁹Synthesized from perrhenic acid and RbOH. See Ref. 13.
- ²⁰See, for example, R. M. Macfarlane, A. Z. Genack, and R. G. Brewer, *Phys. Rev. B* **17**, 2821 (1978).
- ²¹S. Völker, R. M. Macfarlane, A. Z. Genack, H. P. Trommsdorf, and J. H. van der Waals, *J. Chem. Phys.* **67**, 1759 (1977).
- ²²R. H. Pantell and H. E. Puthoff, *Fundamentals of Quantum Electronics* (Wiley, New York, 1969).
- ²³W. W. Rigrod, *J. Appl. Phys.* **34**, 2602 (1963).
- ²⁴P. Kolodner, H. S. Kwok, J. G. Black, and E. Yablonovitch, *Opt. Lett.* **4**, 38 (1979).
- ²⁵W. E. Seward and V. Narayanamurti, *Phys. Rev.* **148**, 463 (1966).
- ²⁶A. Yariv, *Quantum Electronics*, 2nd ed. (Wiley, New York, 1975), p. 173.
- ²⁷R. G. DeVoe and R. G. Brewer, *Phys. Rev. Lett.* **50**, 1269 (1983).
- ²⁸M. V. Klein, in *Physics of Color Centers*, edited by W. B. Fowler (Academic, New York, 1968), p. 527.
- ²⁹D. E. McCumber and M. D. Sturge, *J. Appl. Phys.* **34**, 1682 (1963).
- ³⁰G. Dolling, R. A. Cowley, C. Shittenhelm, and I. M. Thorson, *Phys. Rev.* **147**, 577 (1966).
- ³¹H. W. Moos, *J. Lumin.* **1-2**, 106 (1970).
- ³²A. J. Sievers, R. O. Pohl, A. R. Chraplyvy, D. Pramanik, and G. Schmidt, Annual Technical Progress Report, U. S. Advanced Research Projects Agency, Contract No. F19628-75-C-0177 (July 1976), p. 33 (unpublished).
- ³³H. Dubost, *Ber. Bunsenges. Phys. Chem.* **82**, 112 (1978).
- ³⁴F. Legay, in *Chemical and Biochemical Applications of Lasers*, edited by C. B. Moore (Academic, New York, 1977), Vol. II, pp. 43-86.
- ³⁵H. Dubost and R. Charneau, *Chem. Phys.* **41**, 329 (1979).
- ³⁶H. Dubost, A. Lecuyer, and R. Charneau, *Chem. Phys. Lett.* **66**, 191 (1979).
- ³⁷L. Abouaf-Marguin, H. Dubost, and F. Legay, *Chem. Phys. Lett.* **22**, 603 (1973).
- ³⁸L. Abouaf-Marguin, P. Boissel, and B. Gauthier-Roy, *J. Chem. Phys.* **75**, 495 (1981).
- ³⁹L. Abouaf-Marguin, B. Gauthier-Roy, and F. Legay, *Chem. Phys.* **23**, 443 (1977).
- ⁴⁰L. Abouaf-Marguin and B. Gauthier-Roy, *Chem. Phys.* **51**, 213 (1980).
- ⁴¹B. Gauthier-Roy, L. Abouaf-Marguin, and F. Legay, *Chem. Phys.* **46**, 31 (1980).
- ⁴²A. J. Sievers, *Phys. Rev. Lett.* **13**, 310 (1964); P. G. Dawber and R. J. Elliott, *Proc. Phys. Soc. London* **81**, 453 (1963); D. L. Dexter, *Phys. Rev.* **101**, 48 (1956).
- ⁴³G. Herzberg, *Spectra of Diatomic Molecules* (Van Nostrand/Rienhold, New York, 1950), p. 383.
- ⁴⁴J. M. Ziman, *Principles of the Theory of Solids* (Cambridge University Press, Cambridge, 1972), p. 261.
- ⁴⁵F. Wooten, *Optical Properties of Solids* (Academic, New York, 1972), p. 72.
- ⁴⁶W. M. Kahan, *Hewlett Packard J.* **30**, 20 (1979).
- ⁴⁷D. W. Marquardt, *J. Soc. Ind. Appl. Math.* **11**, 431 (1963).
- ⁴⁸P. R. Bevington, *Data Reduction and Error Analysis for the Physical Sciences* (McGraw-Hill, New York, 1969), p. 237.